Solar Energy 201 (2020) 480–488

Contents lists available at ScienceDirect

Solar Energy

journal homepage: www.elsevier.com/locate/solener

Temperature dependence of Raman scattering in the $Cu_2ZnSnSe_4$ thin films on a Ta foil substrate

A.V. Stanchik[a], M.S. Tivanov[b], I.I. Tyukhov[c,*], R. Juskenas[d], O.V. Korolik[b], V.F. Gremenok[a], A.M. Saad[e], A. Naujokaitis[d]

[a] Scientific and Practical Materials Research Center, National Academy of Sciences of Belarus, 19, P. Brovki St., 220072 Minsk, Belarus
[b] Faculty of Physics, Belarusian State University, 4, Nezavisimosti Av., 220030 Minsk, Belarus
[c] San Jose State University, Department of Mechanical Engineering, One Washington Square, San Jose, CA 95192-0087, USA
[d] State Research Institute Center for Physical Sciences and Technology, 231, Sauletekio Av., 10257 Vilnius, Lithuania
[e] Al-Balqa Applied University, Salt 19117, Jordan

ARTICLE INFO

Keywords:
$Cu_2ZnSnSe_4$
Thin film
Flexible metal substrate
Microstructure
Raman spectroscopy
Temperature dependence

ABSTRACT

The temperature dependence (in range from 24 to 290 K) of Raman spectroscopy of the $Cu_2ZnSnSe_4$ (CZTSe) films with Zn-rich (series **A**) and Zn-poor (series **B**) composition obtained on a Ta foil is investigated. Analisys and approximation by the Lorentz function of the CZTSe Raman spectra suggests that the CZTSe most intense Raman peak consists of two modes (at 192/189 and 194/195 cm^{-1}), which are slightly shifted from each other. In addition, the Raman peaks around 192 and 189 cm^{-1} lead to asymmetric broadening of dominant peaks at 194 and 195 cm^{-1} in Raman spectra of the CZTSe films series **A** and **B**, respectively. In the case of the Sn-rich CZTSe films, we attribute of Raman peak around 189 cm^{-1} to $SnSe_2$ compound. However in the case of the Sn-poor CZTSe films, the observable shift is too high to assign confidently the 192 cm^{-1} band to a $SnSe_2$ compound, which was not detected by XRD analysis. We suppose that this mode is attributed to disordered kesterite structure. The temperature dependence Raman spectra for both series of the CZTSe films shows that a change temperature from 290 to 24 K leads to position shift and narrowing of the CZTSe Raman A-modes. The calculated temperature coefficients and anharmonic constants in Klemens model approximations for temperature dependence of shift position and FWHM of the CZTSe A-modes shown that four-phonon process has dominant contribution in damping process and as a consequence in Raman spectrum changes for two series of the CZTSe films.

1. Introduction

Recently, semiconductor thin films obtained on flexible metal substrates have been of great interest for use in solar cells (Salavei et al., 2016; Chantana et al., 2018; Sim et al., 2018; Zhao et al., 2018; Yan et al., 2019). The flexible metal substrates offer several advantages over heavy breakable glass substrates, which require additional care and significant support in the manufacture and installation of solar cells based on them (Bojic et al., 2016; Kessler et al., 2005; Otte et al., 2006; Pagliaro et al., 2008). Flexible metal substrates make it possible also to apply solar cells to bendable surfaces, use them in Building Integrated Photovoltaic (BIPV) and mobile applications, where weight is important etc. In addition, the use of low-cost flexible metal substrates can help to reduce the cost of solar cells.

Today, the $Cu_2ZnSnSe_4$ (CZTSe) thin films are the most promising as absorbing materials for flexible solar cells. Since the most effective thin-film materials (Green et al., 2018), such as $CuIn_xGa_{1-x}(S,Se)_2$ (CIGSe) and CdTe, have problems associated with the use of low abundance and of toxic raw materials, that could limit the production and economic stability of solar cells based on them. In contrast, the CZTSe thin films consist of abundant and low-toxicity materials (Das et al., 2016). In addition, this material has quite high coefficient of the optical absorption (10^4 cm^{-1}) and nearly optimal band gap value for solar cells application (~1.0 eV) (Das et al., 2016). The record efficiency of the CZTSe solar cells on glass substrate is 11.7% (Tampo et al., 2019), while efficiency of the CZTSe flexible solar cells is 6.48% (Sim and Yang, 2017) and 6.1% (Lopez-Marino et al., 2016) on Mo foil and stainless steel (SS) foil substrates, respectively. At the same time, theoretical efficiency of the CZTSe solar cells is about 30% (Shockley and Queisser, 1961). In addition, Ti (Kaigawa et al., 2015) and Ta foils (Stanchik et al., 2019; Stanchik et al., 2018) were also used as substrates for the CZTSe thin films.

* Corresponding author at: San Jose State University, Department of Mechanical Engineering, One Washington Square, San Jose, CA 95192-0087, USA.
E-mail address: igor.tyukhov@sjsu.edu (I.I. Tyukhov).

https://doi.org/10.1016/j.solener.2020.03.043
Received 12 February 2020; Received in revised form 12 March 2020; Accepted 12 March 2020

The highest efficiency of CZTSe solar cells is low compare with that of theoretical value due to a large number of defects and/or disordering inside CZTSe, as well as the presence of secondary phases. As was noted by Yan et al. (2019), these defects and secondary phases lead to band tailing in absorber and a large recombination occurring near the absorber and substrate interface, what is the main cause for open-circuit voltage (V_{oc}) and fill factor degradation in the CZT(S,Se) solar cells. Therefore, the formation of secondary phases and defects in the CZTSe films must be controlled. It is also worth noting that the highest performing CZTSe solar cells are Cu-poor and Zn-rich (Chen et al., 2013). Therefore, secondary phase/phases like ZnSe, SnSe, $SnSe_2$, and CuSe, should exist in the CZTSe thin films. However, it is very difficult to identify the presence of these secondary phases by X-ray diffraction (XRD). Besides, according to Chen et al. (2009), CZTSe crystallize mainly in the kesterite or stannite crystalline structures, wherein kesterite is thermodynamically the most favourable structure (Maeda et al., 2009). Another possible crystalline structure is disordered kesterite (Lafond et al., 2012), where the Cu and Zn are randomly distributed within the Cu/Zn lattice planes; the difference in binding energy between the kesterite and disordered kesterite structures is about 3 meV/atom. Grossberg et al. (2014) has concluded that the transition from kesterite to disordered kesterite structures can change the effective band gap of the absorber, which in turn affects on the V_{oc} of solar cells. It is very difficult to distinguish between kesterite, stannite and disordered kesterite phases due to their similar XRD patterns.

Raman spectroscopy is one of those techniques which have immense potential in the analysis of crystal structure. This method is extremely sensitive to structural disorder, in this case defined as any kind of modification of the crystalline structure of the material (i.e. stannite or kesterite) and can distinguish other secondary phases in materials with similar crystal structure. According to Dimitrievska et al. (2015, 2019), presence of defects can lead to several types of changes in the Raman spectra, depending on their type and concentration.

As known, Raman spectroscopy provides information regarding optical modes of vibrations due to inelastic light scattering. Therefore, this method is also a unique technique to study the temperature behaviour of materials (Wu et al., 2008), for example, thermal conductivity, as thermal and electrical properties of the semiconductor thin films are affected by anharmonic phonon-phonon interactions. The change of position and linewidth of Raman peaks with respect to temperature can provide fundamental knowledge regarding anharmonicity of vibration (Sarswat et al., 2011). It is also worth noting that at room temperature, the background noise caused by relatively high-energy lattice vibrations makes it difficult to detect phonons (Singh et al., 2014). Temperature dependence Raman investigations have already been reported for various photovoltaic semiconducting materials including CZTS thin films (Sarswat et al., 2011; Singh et al., 2014), but this area is still poorly investigated for the CZTSe thin films (Djemour et al., 2013).

In this work, the temperature dependence of the Raman peaks position and FWHM for CZTSe films obtained on a flexible Ta substrate was investigated in the temperature range of 24–290 K. These analyses are essential for understanding the structural properties and phononic behaviors of this absorbers obtained on metal substrates. But at the present time, there are no experimental works to determine and analyze anharmonic phonon properties of the CZTSe films using Raman spectroscopy.

2. Experimental

2.1. Synthesis of the CZTSe thin films

The CZTSe thin films were produced by the three-stage process (Gremenok et al., 2016; Gremenok et al., 2017). At the first stage, the Cu/Sn/Zn precursors were obtained by sequential electrochemical deposition on a Ta foil substrate in galvanostatic mode with the sequence of Cu, Sn and Zn layers. At the second stage, preliminary annealing of the electrodeposited Cu/Sn/Zn precursors in a tube furnace in an 95% Ar + 5% H_2 atmosphere at 350 °C during 30 min was carried out. Then the Cu/Sn/Zn precursors were selenized in a home-made quartz container (volume 12.5 cm^3) with 5 mg of powdery Se under 1 bar of Ar gas pressure. Selenization was performed at temperatures 580 °C during 30 min.

2.2. Characterization

The SEM characterisation of surface morphology, cross-sections, and EDX analysis of the CZTSe thin films were carried out in a dual beam system FE-SEM-FIB Helios Nanolab 650 (FEI Company) equipped with an x-ray spectrometer X-Max (Oxford Instruments). Ultima IV X-ray diffractometer with monochromatic CuK_α radiation (λ = 0.154078 nm) was used for phase analysis. Analysis of the phase composition was performed with the use of the Crystallography Open Database (COD) by «Match» software package. For the lattice parameters, crystallite size and microstrain of the CZTSe films we used the Rietveld analysis, implemented in the «Material Analysis Using Diffraction» («MAUD») software package (Lutterotti et al., 1999).

Raman spectra were obtained using confocal Raman spectrometer Nanofinder HE at temperature 24–290 K with a spectral resolution better than 0.7 cm^{-1}. During these measurements, the sample was studied in vacuum temperature-controlled cell (pressure less than 5×10^{-4} Pa, temperature setting accuracy of 0.05 K). The Raman spectra were excited with a continuous solid laser emitting at a wavelength of 532 nm with an optical power of 3.0 mW. The diameter of the laser spot at the sample surface was ~1.5 μm.

3. Results and discussion

3.1. Composition and morphology

The elemental composition of the CZTSe thin films is represented in Table 1. The ratios of Zn/Sn and Cu/(Zn + Sn) indicates a deficiency of copper in the both series of CZTSe thin films, as well as an excess and small deficiency of zinc in the CZTSe films series **A** and **B**, respectively.

The CZTSe thin films series **A** and **B** had very different surface morphologies depending on elemental composition (Fig. 1). The micrograph of the CZTSe film series **A** (Fig. 1a) shows two types of crystals. The small crystals have a size of about 400 nm and the size of large crystals is about one micron. In addition, there are few voids on the surface of the CZTSe films series **A**, which are associated with the material loss due evaporation of some volatile elements during the selenization. The micrograph of the CZTSe film series **B** (Fig. 1b) shows

Table 1
The elemental composition and atomic ratios of the CZTSe thin films on a flexible Ta foil.

Series	Atomic percent				Ratio				
	Cu	Zn	Sn	Se	Zn/Sn	Cu/Zn	Cu/Sn	Cu/(Zn + Sn)	Se/metal
A	22.09	18.53	10.83	48.54	1.71	1.19	2.04	0.75	0.94
B	19.47	10.30	16.30	53.93	0.63	1.89	1.19	0.73	1.17

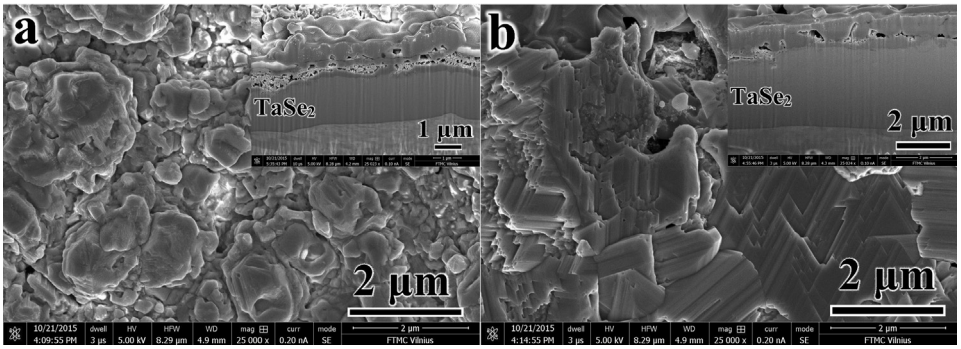

Fig. 1. Top view SEM images of the CZTSe thin films series **A** (a) and **B** (b) on a Ta foil substrate. Insert to (a, b) shows the typical cross-sectional image of the CZTSe thin films series **A** and **B**. The CZTSe thin films series **A** and **B** were Cu-poor, Sn-poor, Zn-rich and Cu-poor, Sn-rich, Zn-poor, respectively.

densely packed with compact faceted grain structure. The thickness of the CZTSe layer in the films of **B** series (Fig. 1a, insert) is slightly less, than of the **A** series (Fig. 1b, insert).

3.2. X-ray diffraction

The XRD patterns of the CZTSe thin films with different elemental composition are shown in Fig. 2. The XRD patterns of the both CZTSe thin films showed the prevalence peak at 2θ = 27.12/27.16° of CZTSe tetragonal phase (Card No.: 96-722-0527) with preferred orientation [1 1 2]. In addition, there are reflections of Ta (Card No.: 00-004-0788) and $TaSe_2$ (Card No.: 00-065-3483) which is formed during the selenization of the CZTSe films. Besides, both of the CZTSe thin films can contain ZnSe and Cu_2SnSe_3 phases. But XRD-peaks of ZnSe and Cu_2SnSe_3 phases overlap with the highest intensity peaks of CZTSe thus their are difficult to distinguish by a conventional XRD technique. According to the quasi ternary phase diagram of CZTSe (Schorr et al., 2020; Mousel et al., 2013), the total composition of the CZTSe films series **A** is found to be Zn-rich located on the Cu-poor side of the ZnSe-Cu_2SnSe_3-tie line, while the total composition of the CZTSe films series **B** is found to lie in the Zn-rich and Sn-rich regions of the phase diagram. In both cases, the compositions of the CZTSe films correspond to the region of the phase diagram which assumes the coexistence of CZTSe, $SnSe_2$ and ZnSe phases. Nevertheless, it can be noted that ZnSe (Card N.: 96-900-8858) phase should exist in the CZTSe thin films series **A** as these films were Zn-rich, while the existence of the ZnSe phase in the films of **B** series (Zn-poor) is unlikely (Just et al., 2016). At the same time, the existence of $SnSe_2$ phase in the films of **A** series (Sn-poor) is unlikely, while its existence in the films of **B** series (Sn-rich) is possible. Nevertheless, Drabavičius et al. (2020) found the existence of the ZnS phase in the Zn-poor CZTS films by Raman spectroscopy using an excitation wavelength of 325 nm. The Raman spectra revealed that the Zn-rich CZTS films possessed the largest quantity of ZnS secondary phase while the Zn-poor films possessed the lowest one.

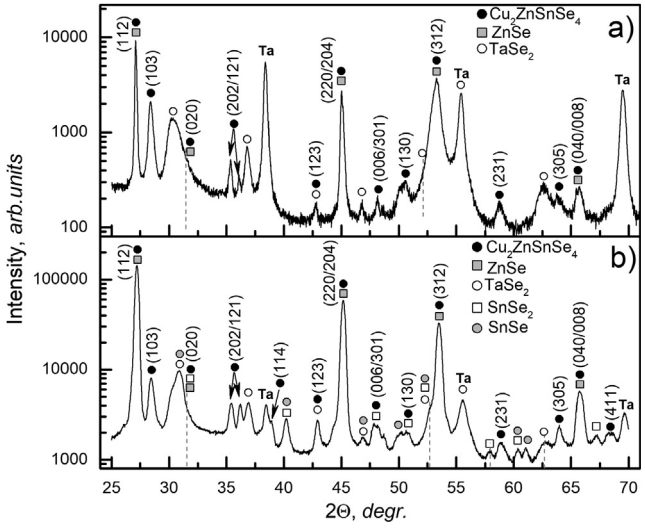

Fig. 2. The XRD patterns of the CZTSe thin films series **A** (a) and **B** (b) on a Ta foil substrate. The CZTSe thin films series **A** and **B** were Cu-poor, Sn-poor, Zn-rich and Cu-poor, Sn-rich, Zn-poor, respectively.

According to Vauche et al. (2016b), the SnSe and $SnSe_2$ secondary phases can be detected at the surface of the CZTSe thin films by XRD. The XRD peak around 31° indicates the presence of SnSe and/or $SnSe_2$, because this peak is the most intense XRD peak of SnSe and $SnSe_2$ (Vora et al., 2012; Yoo et al., 2013). Nevertheless, in our case this peak coincides or is very close to those of CZTSe and $TaSe_2$, and can be attributed to CZTSe and $TaSe_2$ phases (Fig. 2b). Therefore, low intensity reflections at 40.2, 58.2, 60.4, 61.06, 62.7, and 67.23° (Fig. 2b) which can not be attributed to the CZTSe phase could point to the presence of SnSe (Card No.: 03-065-3811) and/or $SnSe_2$ (Card No.: 00-023-0602). According to Vauche et al. (2016a), characteristic SnSe and/or $SnSe_2$ grains are observed on surfaces of many CZTSe thin films with Sn-rich and Cu-poor composition (i.e., when ratios of Zn/Sn < 1) which explains the formation of the faceted grain structure of the CZTSe films series **B** with hightly Sn-rich composition (Fig. 1b). Thus, it can be suggested that such phases as SnSe or/and $SnSe_2$ exist in the CZTSe films series **B**.

It should be noted that the $TaSe_2$ layer in the CZTSe films series **B** is much more thicker than of the **A** series (Fig. 1). According to Yao et al. (2016), the $MoSe_2$ layer forms at the CZTSe/Mo interface when the metal precursor of the CZTSe films contains excess Sn and the SnSe- or/and $SnSe_2$-containing phase in the CZTSe thin films may have catalyzed the formation of $MoSe_2$ layer. Taking this into consideration, it can be concluded that the $TaSe_2$ layer have similar formation features at the CZTSe/Ta interface in the CZTSe thin films depending on the Sn content.

The determined values of lattice parameters, coherent scattering region (D), microstrain (ε), and dislocation density (δ) by «MAUD» software package are shown in Table 2. As can be seen, the resulting volume of the CZTSe is a slightly larger than the theoretical one. The CZTSe films of **A** series have a volumetric expansion of up to 0.44% while the CZTSe films of **B** series have a volumetric expansion of up to 0.33%. It is known that the CZTSe can crystallize into the kesterite or stannite structure, and the partially disordered kesterite, which can lead to a volumetric expansion of up to 0.3% (Schorr, 2007) mainly by the increase of c (Marquez et al., 2016). The FWHM of the CZTSe 112 peak increases with decrease in Zn/Sn ratio. Such change indicates an improvement in the crystallinity of the CZTSe films series **A**, which is consistent with the increase in grain size.

The dislocation density of the CZTSe thin films was determined from the following relation (Henry et al., 2018):

Table 2
The lattice parameters, full-width at half-maximum (FWHM) of 112 main peak, coherent scattering region (D), dislocation density (δ), and microstrain (ε) of the CZTSe thin films series **A** and **B** on a Ta foil substrate.

Series	The lattice parameters of CZTSe			FWHM (1 1 2)	D, nm	δ	ε
	a, Å	c, Å	V				
A	5.699 ± 0.001	11.345 ± 0.003	368.470	0.14359	12.248 ± 1.566	0.007	0.0015 ± 0.0001
B	5.691 ± 0.002	11.364 ± 0.005	368.051	0.35216	1.707 ± 0.136	0.343	0.0028 ± 0.0001
The theoretical data	5.6882 (Card N.: 96-153-1983)	11.3378	366.842	–	–	–	–

$$\delta = 1/D^2. \quad (1)$$

As can be seen, the CZTSe thin film series **B** had higher values of dislocation density and microstrain than the CZTSe film series **A** (Table 2). The decrease of the values of strain and dislocation density was attributed to changes of the crystallite size and with increase of the film thickness. It is known that a number of sources can cause microstrain in crystallites: dislocation (most important source), vacancies, shear planes etc. (Lifshin, 2008).

3.3. Raman spectroscopy

The Raman spectra of the CZTSe thin films series **A** and **B** measured at different temperatures are shown in Figs. 3 and 4, respectively. The Raman spectra of the both series of the CZTSe films are very similar. The Raman peaks around 79/80, 170/171, 194/195, 221, 232/231, and 242 cm^{-1} belong to the E (TO LO) mode, A mode (labelled as A^{1A}/A^{1B}), A mode (labelled as A^{2A}/A^{2B}), A mode, E (TO LO), and B (TO LO) mode of the CZTSe with the kesterite structure (Gürel et al., 2011; Khare et al., 2012), respectively. Signal around near 250 cm^{-1} (FWHM = 5.38/4.15 cm^{-1}) belonging to the ZnSe cubic (Salome et al., 2014) is found in the Raman spectra of the CZTSe films series **A** and **B**. Besides, the Raman peak at 209 cm^{-1} (FWHM = 2.72 cm^{-1}) was observed in the Raman spectra of the films **B** series (Fig. 4d), which corresponds to the ZnSe cubic too (Salome et al., 2014). The ratios of intensity Raman paek at 250 cm^{-1} to the dominant Raman peak at 194/195 cm^{-1} for the CZTSe films series **A** and **B** are ~10 and ~29, respectively. The low intensity of the detected Raman peaks at 250 cm^{-1} compared to dominant Raman peak of the CZTSe is apparently associated with weak contribution of this mode under standard Raman scattering conditions (514–532 nm) (Dimitrievska et al., 2019) and/or with the low overall amount of ZnSe formed on the surface of the CZTSe films investigated. For example, Fairbrother et al. (2014) found a Raman peak at 248–250 cm^{-1} with low intensity on the Raman spectra of Zn-rich CZTSe films using excitation wavelength of a 514 nm. This peak was assigned to ZnSe phase, what is confirmed by Raman scattering measurements performed with a 457.9 nm excitation wavelength (this wavelength corresponds to resonant excitation conditions for this compound). In our earlier work (Stanchik et al., 2019), it was established using SIMS that the ZnSe secondary phase in the Zn-rich CZTSe films is formed on the back side of the films. It explains the weak intensity of Raman peaks from ZnSe in the Raman spectra. It should be noted that the inclusions of ZnSe grains on the back of the absorbers (CZTSe film) does not affect the efficiency of solar cells, as it can be expected from the ZnSe layer or its inclusion grains on the surface of the absorbers (Hsu et al., 2013; Bishop et al., 2013). In the Raman spectra of the CZTSe thin films series **B** with Zn/Sn < 1 a signal around 68 and 129 cm^{-1} belonging to the SnSe orthorhombic (Salome et al., 2014) was not detected. No spectroscopic evidence for presence of $TaSe_2$ phase was obtained in the Raman spectra of the both CZTSe thin films (Hajiyev et al., 2013).

It can be seen from the Raman spectra of the both CZTSe thin films (Figs. 3 and 4) that in all cases the dominant Raman peak of the CZTSe is asymmetrically broadened towards the smaller Raman shift. The use

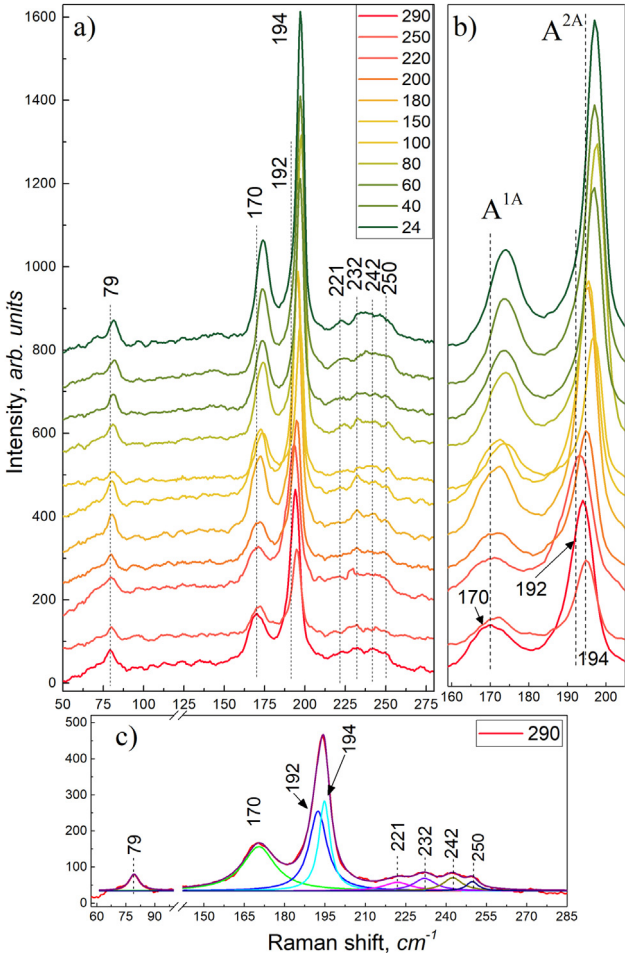

Fig. 3. Raman spectra of the CZTSe thin films series **A** on a Ta foil in the temperature range of 24–290 K (a). The inserts (b) and (c) present fragments of the Raman spectra in the wavenumber region of 159–205 cm^{-1}, and fragments of the Raman spectra approximated by the Lorentz function in the the wavenumber region of 59–295 cm^{-1}, respectively. The green line (c) shows the sum of the fits. All Raman spectra are measured with a 532 nm excitation wavelength. (For interpretation of the references to colour in this figure legend, the reader is referred to the web version of this article.)

of two Lorentzian curves in our cases shows good quality of the fit for dominant Raman peak of the CZTSe and fit his the asymmetry (Figs. 3c and 4c). This results gives evidence that two modes at 192/189 cm^{-1} (FWHM = 8.15/8.99 cm^{-1}) and 194/195 cm^{-1} (FWHM = 4.19/5.14 cm^{-1}) are present in the our spectra of the CZTSe films series **A** and **B**, but with an diverse intensity depending on elemental composition.

A similar asymmetrically broadening dominant Raman peak of the CZTSe was observed in few works (Khare et al., 2012; Djemour et al., 2013; Juskenas et al., 2016; Rey et al., 2014; Schelhas et al., 2017). For

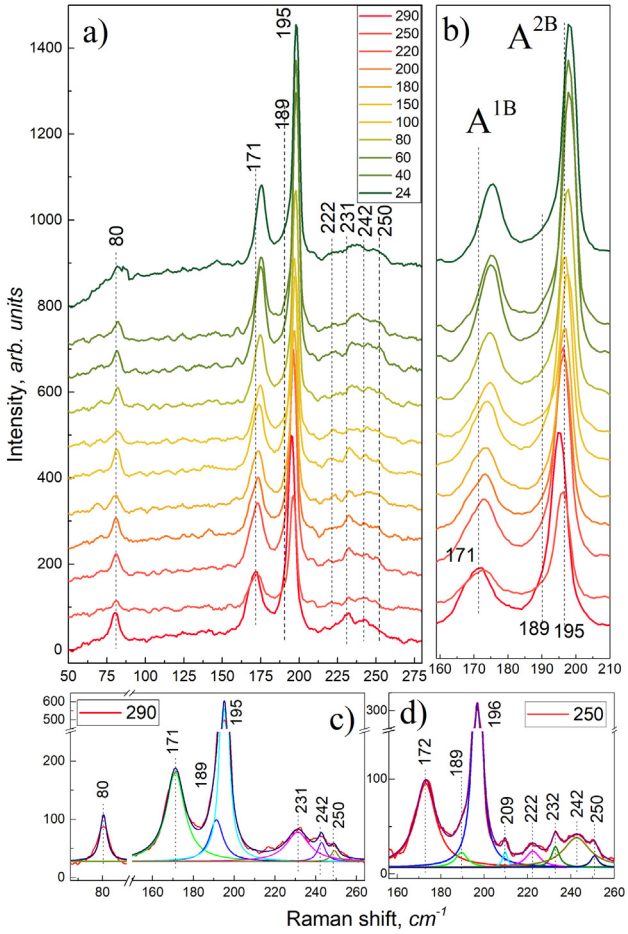

Fig. 4. Raman spectra of the CZTSe thin films series **B** on a Ta foil in the temperature range of of 24–290 K (a). The inserts (b), (c), and (d) present fragments of the Raman spectra in the wavenumber region of 159–210 cm^{-1}, fragments of the Raman spectra approximated by the Lorentz function in the the wavenumber region of 63–261 cm^{-1}, and 160–260 cm^{-1}, respectively. The green line (c, d) shows the sum of the fits. All Raman spectra are measured with a 532 nm excitation wavelength. (For interpretation of the references to colour in this figure legend, the reader is referred to the web version of this article.)

example Djemour et al. (2013) found what a inhomogeneous laser heating affects does not cause the asymmetrical broadening dominant Raman peak of the CZTSe in the CZTSe thin films. Moreover, Djemour et al. (2013) noted that if the contribution of the low intense peak near dominant Raman peak of the CZTSe can be clearly discerned, then the peak shape in Raman spectrum of the CZTSe films, where it does not occur is clearly due to broadening and not due of second line. However, the assignment of this second line is not obvious. Nevertheless, according to Khare et al. (2012), Fontane et al. (2012), Djemour et al. (2013), and Dimitrievska et al. (2014) this second line is associated to a different crystal modification (like, stannite and Cu-Au ordering) or the phonon confinement effects because of the presence of lattice defects in the scattering volume (for example, disordered kesterite). In addition, a similar broadening and shift towards greater Raman shift of the CZTSe dominant Raman peak was observed at studying the structural transition in the cation sublattice of CZTSe (i.e., transitioning from disordered to ordered kesterite) by Rey et al. (2014) and Schelhas et al. (2017). Nevertheless, the existence of this second line at dominant Raman peak of the CZTSe is not discussed in these works, but it has been established that the disordered keserite leads to asymmetric broadening and shift of peak towards greater Raman shift.

So, combining the above results, the asymmetric broadening dominant Raman peak of the CZTSe for the CZTSe films series **A** and **B** occurs due to the contribution the second line at 192 and 189 cm^{-1}, respectively. However, the signals at 192 and 189 cm^{-1} are possibly associated with $SnSe_2$ (hexagonal) and/or polycrystalline Cu_2SnSe_3, which are characterized by the most intense Raman peak at 185 and 180 cm^{-1}, respectively. For example, Juskenas et al. (2016) suggested that the detected signal at 189 cm^{-1} is associated different crystal modification (stannite) or disordered kesterite, since the observed shift between 189 and 185 ($SnSe_2$) or 180 cm^{-1} (Cu_2SnSe_3) is too large to confidently assign a signal at 189 cm^{-1} phases of $SnSe_2$ or Cu_2SnSe_3. Nevertheless, Vauche et al. (2016b) has report, wherein the detected Raman signal around 188 cm^{-1} is attributed to SnSe/$SnSe_2$ phase, at the same time this phase was detected using X-ray analysis in the investigated samples. According to Vauche et al. (2016b), signal around 188 cm^{-1} disappear on the Raman spectra after $(NH_4)_2S$ etching, which is used to remove Sn-Se phases from surface of the CZTSe thin films. In addition, the Sn-Se secondary phases are not detected by X-ray analysis in samples after etching. Therefore, Vauche et al. (2016b) confidently attributed the signal around 188 cm^{-1} to the SnSe/$SnSe_2$ phase. Thus, in the first case, the second line at 192 cm^{-1} is possibly associated with disordered kesterite crystalline structure or phonon confinement effects, due to the large discrepancy in the position of the Raman peak from $SnSe_2$. On contrary, in the second case, the line at 189 cm^{-1} belongs to $SnSe_2$, which was detected by X-ray analysis. This result indicates that $SnSe_2$ exists in the CZTSe thin films of **B** series.

According to Lafond et al. (2012) and Valle-Rios et al. (2016), defect complex [$2Zn_{Cu}$ + Zn_{Sn}] is expected in compositional range of the CZTSe films series **A**, while defect complex [$2V_{Cu}$ + Sn_{Zn}] or [Sn_{Cu} + V_{Cu} + V_{Zn}] is expected in compositional range of the CZTSe films series **B**. As it was shown by Scragg et al. (2015) and Schorr et al. (2020), high concentration of defects [Cu_{Zn} + Zn_{Cu}] is the result of the disordering of Cu and Zn in the Cu-Zn layer of CZTSe kesterite. On contrary, the presence of Sn_{Zn} point defects lead to appearance of an additional SnSe-like contribution around the 185 cm^{-1} frequency region. This is consistent with our assumptions of the second line at 192 and 189 cm^{-1}.

In the presented Figs. 3c and 4c, it is seen that a change in the intensitiy of the Raman peaks at 170/171 cm^{-1} and of the 234–250 cm^{-1} spectral region (related to the contribution of 232, 242 and 250 cm^{-1} Raman modes) observed depending on the elemental composition of the CZTSe films. According to Márquez-Prieto et al. (2015) the intensity ratio of two dominant Raman peaks of the CZTSe is very sensitive to the Cu content in the CZTSe thin films, particularly when there was Cu deficit (Cu/(Zn + Sn) < 1). In our case, the intensity ratios of the modes A^{1A} to A^{2A} and A^{1B} to A^{2B} for the CZTSe films series **A** and **B** are ~2.7 and ~3.1, respectively, and do not change basically with decreasing temperature. As can be seen, an intensity ratio of the CZTSe modes for the films of **B** series is slightly larger compared to **A** series, since the ratio Cu/(Zn + Sn) for the CZTSe films series **B** is slightly smaller than for the **A** series (Table 2). Furthermore, an increase in relative intensity of peak around 170/171 cm^{-1} in Raman spectra for the CZTSe films of **B** series compared to **A** series (Table 1) is observed. According to Mortazavi Amiri and Postnikov (2010), the broad Raman peak at 170/171 cm^{-1} (A^{1A}/A^{1B}) due to the convolution of two A modes and two B modes which include Se vibrations and Cu/Zn and Cu/Sn atomic plane vibrations, while the peak at 194/195 cm^{-1} (A^{2A}/A^{2B}) involves purely Se anion vibrations. Since the A-modes correspond to only Se vibrations, no changes in their intensity are expected with changes in cation composition. Accordind to Chen et al. (2013), this change is possibly due to an increase in the concentration of a cluster defects [V_{Cu} + Zn_{Cu}], which present in the Cu-poor CZTSe films and do not affected by the B-type defect cluster concentration ([$2Zn_{Cu}$ + Zn_{Sn}]). Moreover, Dimitrievska et al. (2019) suggested that increasing concentration of V_{Cu} lead to an increased area of Raman peak at 176 cm^{-1}, while an increase of Zn_{Cu} defects have a residual influence on the area of the peak. Thus, considering that composition of the CZTSe thin films series **A** corresponds to the B-type line with most

expected [$2Zn_{Cu}$ + Zn_{Sn}] defect complexes (Lafond et al., 2012), while composition of the CZTSe thin films series **B** corresponds to the E-type line with most expected [$2V_{Cu}$ + Sn_{Zn}] or [Sn_{Cu} + V_{Cu} + V_{Zn}] defect complexes (Valle-Rios et al., 2016). It can be concluded that with a decrease in Cu content and concomitant increase of V_{Cu} defects in the CZTSe films series **B** compared to series **A** lead to increases in overall relative intensity of the B-symmetry mode at 170/171 cm^{-1}.

As can be seen, the relative intensity of the Raman peak at 250 cm^{-1} increases with increasing Zn content in the CZTSe thin films. The observed change in intensity of the mode at 250 cm^{-1} of the CZTSe films is difficult to study due to the contribution of the mode at 242 cm^{-1} (Dimitrievska et al. 2019). Nevertheless, accordind to Dimitrievska et al. (2015) this can be associated with an increase in density of V_{Cu} and Zn_{Sn} point defects, which lead to an increase in the number of Zn-Se bonds and to transformation of the -Sn-Se-Cu-Se-Sn vibrational chains into -ZnSn-Se-Cu-Se-ZnSn-, respectively, for which vibrations is expected in the 250 cm^{-1} region. However, the Zn_{Sn} and V_{Cu} point defects are present in the CZTSe films of **A** and **B** series. In the later work, Dimitrievska et al. (2019) suggested that the Raman peak at 250 cm^{-1} is mostly related to vibrations of the Sn atoms with a possible contribution from vibrations of Zn atoms. This means that the intensity of the Raman mode ZnSe depends on the content of Zn and Sn in the CZTSe films and further research is needed.

3.4. Temperature dependence of Raman shift and linewidth

The temperature change from 290 to 24 K leads to a shift of peaks position towards greater Raman shift (Figs. 3 and 4) and their narrowing in linewidth (FWHM). For a detailed analysis of the Raman spectra obtained at different temperatures, we focus on the two Raman modes with A-symmetry labelled as A^{1A}/A^{1B} and A^{2A}/A^{2B} (Figs. 3 and 4 insert b). The shift of A^{1A}/A^{1B} and A^{2A}/A^{2B} Raman modes were 3.6/4.1 cm^{-1} and 2.8/3.0 cm^{-1}, respectively. The narrowing of FWHM of A^{1A}/A^{1B} and A^{2A}/A^{2B} Raman modes were 6.3/4.4 cm^{-1} and 1.1/1.5 cm^{-1}, respectively.

The temperature dependence of shift position and FWHM for two Raman CZTSe modes were studied by the approximation with linear model and Klemens model equations presented below. According to the linear model the temperature dependence of shift position and FWHM of Raman modes can be described with the Eqs. (2) and (3) (Lu et al., 2018). The fit of Eqs. (2) and (3) to experimental data is shown in Figs. 5 and 6.

$$\omega(T) = \omega_0 + \chi_{RS} \cdot T, \tag{2}$$

$$\Gamma(T) = \Gamma_0 + \chi_{FWHM} \cdot T, \tag{3}$$

where ω_0 is the optical phonon frequency at 0 K, Γ_0 is FWHM for Raman modes at 0 K, χ_{RS} and χ_{FWHM} are temperature coefficients of shift position and FWHM, respectively. The values of ω_0 and Γ_0 were obtained by extrapolation of $\omega(T)$ and $\Gamma(T)$ to T = 0 K, respectively (Figs. 5 and 6).

The calculated temperature coefficients for Raman modes A-symmetrical of the CZTSe are presented in Table 3. The results of linear approximation of shift position and FWHM temperature dependence show that χ_{RS} and χ_{FWHM} for A^{1A}/A^{1B} modes are little bigger than for A^{2A}/A^{2B} one. This indicates that the the four-phonon is the dominant damping process. In addition the results obtained shows that a shift position and FWHM of Raman modes A-modes for CZTSe with temperature is due to of their negative and positive temperature coefficients, respectively.

It is interesting to note that the χ_{RS} for both series of the CZTSe thin films are close, while the χ_{FWHM} for the CZTSe films series **A** compared to series **B** is roughly 1.7 times larger. The origin of such a change in the χ_{FWHM} is not entirely clear and requires further research. It is possibly the result of affected more significantly by the defects; it can change the physical properties of the material and as the result the alteration of pure temperature and volumetric effects.

It is widely known that two effects influence the temperature dependence of Raman spectrum: the thermal expansion and the anharmonic coupling to phonons of other branches (Wang et al., 2008). Typical Klemens model takes into account both phonon-phonon interactions and thermal expansion of the film and substrate (Wang et al., 2008). In our work, the second factor was not taken into account since the layer of the CZTSe thin films is rather thick (about 1 μm, Fig. 1). For example, such calculations were already done for graphene (Kolesov et al., 2019), molybdenum disulfide (Najmaei et al., 2013), and germanium selenide (Deringer et al., 2014).

To describe temperature dependence of shift position $\omega(T)$ and FWHM $\Gamma(T)$ of Raman modes A- symmetrical for the CZTSe films in Klemens model, we used Eqs. (4) and (5), respectively (Deringer et al., 2014; Taube et al., 2016).

$$\omega(T) = \omega_0 + A\cdot[1 + 2/(\exp x - 1)] + B\cdot[1 + 3/(\exp y - 1) + 3/(\exp y - 1)^2], \tag{4}$$

$$\Gamma(T) = \Gamma_0 + C\cdot[1 + 2/(\exp x - 1)] + D\cdot[1 + 3/(\exp y - 1) + 3/(\exp y - 1)^2], \tag{5}$$

where ω_0 and Γ_0 are the energy of optical phonon and FWHM at T = 0 K, respectively; $x = \hbar\omega/2k_BT$, $y = \hbar\omega/3k_BT$, where $\hbar$ is the Planck constant, ω is the frequency, k_B is is the Boltzmann constant, where A, C and B, D are anharmonic constants related to three- and four-phonon processes, respectively.

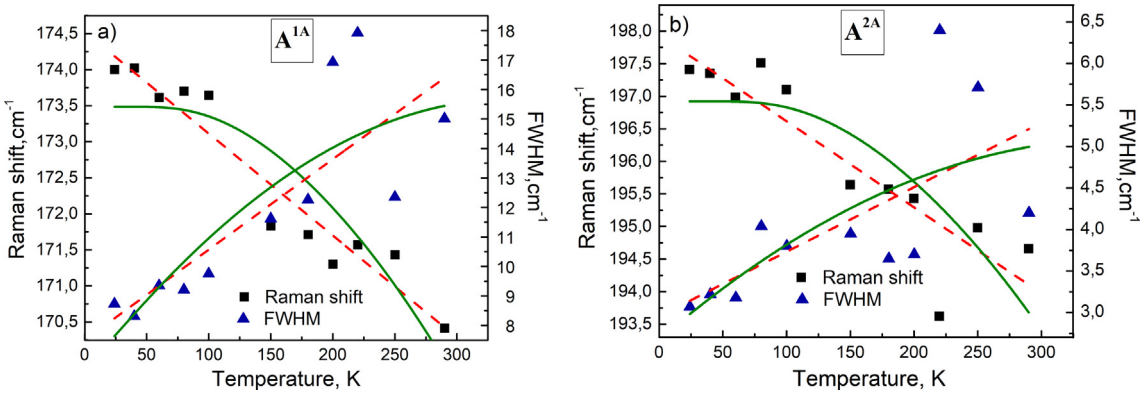

Fig. 5. Linear (dash red line) and Klemens model (green curve) approximations for temperature dependence of shift position and FWHM of A^{1A} (a) and A^{2A} (b) modes for Raman spectra of the CZTSe thin films series **A**. (For interpretation of the references to colour in this figure legend, the reader is referred to the web version of this article.)

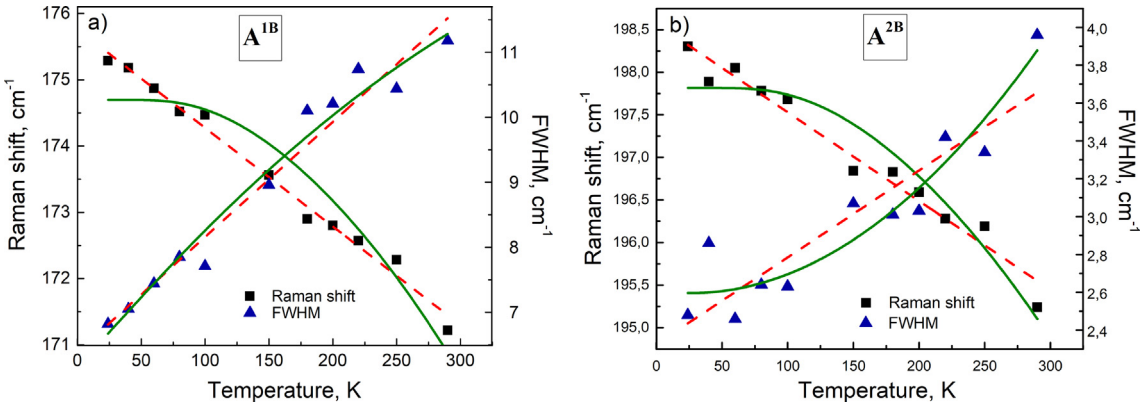

Fig. 6. Linear (dash red line) and Klemens model (green curve) approximations for temperature dependence of shift position and FWHM of A^{1A} (a) and A^{2A} (b) modes for Raman spectra of the CZTSe thin films series **B**. (For interpretation of the references to colour in this figure legend, the reader is referred to the web version of this article.)

Table 3
The calculated values of ω_0 and Γ_0, as well as temperature coefficients of shift position (χ_{RS}) and FWHM (χ_{FWHM}) for A^{1A}/A^{1B} and A^{2A}/A^{2B} Raman A-modes of the CZTSe thin films.

Series of the CZTSe films	Mode	ω_0, cm^{-1}	Γ_0, cm^{-1}	χ_{RS}, cm^{-1}/K	χ_{FWHM}, cm^{-1}/K
A	A^{1A}	174.5	7.5	−0.014	0.031
	A^{2A}	197.9	3.0	−0.013	0.008
B	A^{1B}	175.8	6.4	−0.015	0.018
	A^{2B}	198.6	2.3	−0.010	0.005

The Klemens model approximations of $\omega(T)$ and $\Gamma(T)$ for Raman A-modes of the CZTSe thin films series **A** and **B** are presented on Figs. 5 and 6 (green curve), respectively. It was revealed that temperature dependence of shift position and FWHM for Raman A-modes of the both films series have non-linear character as these dependence are better approximated with Klemens model than with linear one. Moreover, the approximation curve fits well to experimental data, thus confirming that anharmonic phonon-phonon interactions were responsible for the temperature dependence of the CZTSe films Raman spectra.

The calculated values of *A*, *B*, *C* and *D* coefficients in Klemens model are presented in Table 4. In all cases, the values of the *A* and *D* anharmonic coefficients are smaller than *B* and *C*, respectively, thus confirming that the four-phonon process has dominant contribution in damping process and is the main factor responsible for the observed shift position and linewidth variation (FWHM) of Raman modes. For example, Sarswat et al. (2011) also found that the four-phonon process is responsible for the shift position and linewidth of Raman A-mode for kesterite CZTS films.

It is interesting to note that the *C* and *D* anharmonic constants are greater for the CZTSe films of series **A** compared to series **B**. A similar behavior was observed for temperature coefficients χ_{RS} and χ_{FWHM} (Table 3) of Raman A-modes of the CZTSe depending on the composition. Therefore, we assume that there is a dependence of both temperature coefficients and angoramanic constants on the elemental composition of the CZTSe thin films and that requires additional research.

Table 4
The calculated values of *A*, *B*, *C* and *D* coefficients in Klemens model approximations for temperature dependence of shift position and FWHM of the Raman modes for the CZTSe thin films.

Series of the CZTSe thin films	Mode	*A*, cm^{-1}	*B*, cm^{-1}	*C*, cm^{-1}	*D*, cm^{-1}
A	A^{1A}	2.762	−3.947	0.653	−0.007
	A^{2A}	3.668	−4.936	0.068	$-2.817 \cdot 10^{-4}$
B	A^{1B}	3.471	−4.414	0.276	−0.002
	A^{2B}	3.729	−4.274	−0.001	$-2.727 \cdot 10^{-4}$

4. Conclusions

In this work, the temperature dependence of Raman spectra for the CZTSe thin films with Zn-rich, Sn-poor (series **A**) and Zn-poor, Sn-rich (series **B**) compositions is studied in the temperature range of 290–24 K. The CZTSe thin films were produced on flexible Ta foils by a three-stage process. X-ray phases analysis of the CZTSe thin films shows the presence of CZTSe basic phase. The existence of ZnSe phase in the both CZTSe films was confirmed by Raman spectroscopy. In addition, the $SnSe_2$ phase was detected in the CZTSe films series **B** using the X-ray and Raman spectroscopy. It is found that the CZTSe thin films have kesterite or disordered kesterite structure with the lattice parameters close to the theoretical values. In all Raman spectra of the CZTSe films, the dominant Raman peak of the CZTSe is asymmetrically broadened due to the second line. In the Zn-rich CZTSe films, the existence of the second line is attributed to disordered kesterite structure; on contrary, for the Sn-rich CZTSe films, the second line is attributed to the $SnSe_2$ phase, which was detected by X-ray analysis too. A change in the intensitiy of the Raman peaks at 170/171 cm^{-1} and in spectral region of the 234–250 cm^{-1} for the CZTSe films series **A** and **B** are due to the formation of cluster defects depending on the elemental composition of the films. Temperature change from 290 to 24 K leads to a shift of the Raman peaks towards the greater Raman shift and a narrowing in the linewidth (FWHM). It was established that the four-phonon process is the main factor responsible of the observed changes in the Raman spectra of the CZTSe thin films. Dependence of temperature coefficients and anharmonic constants on the elemental composition of the CZTSe thin films has been suggested.

Declaration of Competing Interest

The authors declare that they have no known competing financial interests or personal relationships that could have appeared to influence the work reported in this paper.

Acknowledgments

This work was supported by the Belarusian Republican Foundation for Fundamental Research (grant number T19M-022) and the Belarusian State Programme for Research «Physical material science, new materials and technologies».

References

Bishop, D.M., McCandless, B.E., Mangan, T.C., Dobson, K., Birkmire, R., 2013. Effects of growth conditions on secondary phases in CZTSe thin films deposited by coevaporation. Mater. Res. Soc. 1538, 75–82.

Bojic, M., Radulovic, J., Rankovic, V., Nikolic, D., Bojic, L., Skerlic, J., 2016. Flexible thin-film solar photovoltaics: research and application. Int. J. Eng. 37–40.

Chantana, J., Teraji, S., Watanabe, T., Minemotoa, T., 2018. Influences of Fe and absorber thickness on photovoltaic performances of flexible Cu(In, Ga)S_e2 solar cell on stainless steel substrate. Sol. Energy 173, 126–131.

Chen, S., Gong, X.G., Walsh, A., Wei, S.H., 2009. Crystal and electronic band structure of Cu_2ZnSnX_4 (X = S and Se) photovoltaic absorbers: first-principles insights. Appl. Phys. Lett. 94, 041903.

Chen, S., Walsh, A., Gong, X.G., Wei, S.H., 2013. Classification of lattice defects in the kesterite Cu_2ZnSnS_4 and Cu_2ZnSnS_4 earth-abundant solar cell absorbers. Adv. Mater. 25, 1522–1539.

Das, S., Mandal, K.C., Bhattacharya, R.N., 2016. Earth-Abundant Cu2ZnSn(S,Se)4 (CZTSSe) Solar Cells. In: Paranthaman, M.P., Wong-Ng, W., Bhattacharya, R.N. (Eds.), Semiconductor Materials for Solar Photovoltaic Cells, Switzerland, pp. 25–74.

Deringer, V.L., Stoffel, R.P., Dronskowski, R., 2014. Vibrational and thermodynamic properties of GeSe in the quasiharmonic approximation. Phys. Rev. B 89, 094303.

Dimitrievska, M., Fairbrother, A., Perez-Rodrıguez, A., Saucedo, E., Izquierdo-Roca, V., 2014. Raman scattering crystalline assessment of polycrystalline Cu_2ZnSnS_4 thin films for sustainable photovoltaic technologies: phonon confinement model. Acta Mater. 70, 272–280.

Dimitrievska, M., Fairbrother, A., Saucedo, E., Pérez-Rodríguez, A., Izquierdo-Roca, V., 2015. Influence of compositionally induced defects on the vibrational properties of device grade $Cu_2ZnSnSe_4$ absorbers for kesterite based solar cells. Appl. Phys. Lett. 106, 073903.

Dimitrievska, M., Oliva, F., Guc, M., Giraldo, S., Saucedo, E., Perez-Rodrıguezad, A., Izquierdo-Roca, V., 2019. Defect characterisation in $Cu_2ZnSnSe_4$ kesterites via resonance Raman spectroscopy and the impact on optoelectronic solar cell properties. J. Mater. Chem. A 7, 13293.

Djemour, R., Redinger, A., Mousel, M., Gütay, L., Fontane, X., Izquierdo-Roca, V., Perez-Rodríguez, A., Siebentritt, S., 2013. The three A symmetry Raman modes of kesterite in $Cu_2ZnSnSe_4$. Opt. Express 21 (S4), A695.

Drabavičius, A., Naujokaitis, A., Stalnionis, G., Giraitis, R., Mockus, Z., Kanapeckaitė, S., Kalinauskas, P., Nedzinskas, R., Niaura, G., Jušknėnas, R., 2020. Photoelectrochemical, Raman spectroscopy, XRD and photoluminescence study of disorder in electrochemically deposited kesterite thin film. J. Alloys Compd. 824, 153853.

Fairbrother, A., Fontané, X., Izquierdo-Roca, V., Placidi, M., Sylla, D., Rodriguez, M.E., López-Mariño, S., Pulgarín, F.A., Vigil-Galán, O., Pérez-Rodríguez, A., Saucedo, E., 2014. Secondary phase formation in Zn-rich $Cu_2ZnSnSe_4$-based solar cells annealed in low pressure and temperature conditions. Prog. Photovolt.: Res. Appl. 22, 479–487.

Fontane, X., Izquierdo-Roca, V., Saucedo, E., Schorr, S., Yukhymchuk, V.O., Valakh, M.Y., Pérez-Rodríguez, A., Morante, J.R., 2012. Vibrational properties of stannite and kesterite type compounds: Raman scattering analysis of Cu_2(Fe, Zn)Sn_S4. J. Alloys Compd. 539, 190–194.

Green, M.A., Hishikawa, Y., Dunlop, E.D., Levi, D.H., Hohl-Ebinger, J., Yoshita, M., Ho-Baillie, A.W.Y., 2018. Prog. Photovoltaics Res. Appl. 27 (1), 3–12.

Gremenok, V.F., Juskenas, R., Bashkirov, S.A., Tyukhov, I.I., Kim, W.Y., Chai, S.H., 2016. $Cu_2ZnSnSe_4$ thin films on flexible substrates for solar cells application. Res. Agric. Electric Eng. 4 (2), 39–42.

Gremenok, V.F., Juskenas, R., Petlitskaya, T.V., Stanchik, A.V., Bashkirov, S.A., Giraitis, R., Selskis, A., Pyatlitski, A.N., Solodukha, V.A., Berthold, C., Nickel, K., 2017. Growth and properties of $Cu_2ZnSnSe_4$ films on flexible metallic substrates. In: Proceedings of the 33rd European Photovoltaic Solar Energy Conference and Exhibition, pp. 1081–1084.

Grossberg, M., Krusto, K.J., Raadik, T., Kauk-Kuusik, M., Raudoja, J., 2014. Photoluminescence study of disordering in the cation sublattice of Cu2ZnSnS4. Curr. Appl. Phys. 14, 1424–1427.

Gürel, T., Semik, C., Cagin, T., 2011. Characterization of vibrational and mechanical properties of quaternary compounds Cu_2ZnSnS_4 and $Cu_2ZnSnSe_4$ in kesterite and stannite structures. Phys. Rev. B 84, 205201.

Hajiyev, P., Cong, C., Qui, C., Yu, T., 2013. Contrast and Raman spectroscopy study of single- and few-layered charge density wave material: 2H-$TaSe_2$. Sci. Rep. 3, 2593.

Henry, J., Mohanraj, K., Sivakumar, G., 2018. Photoelectrochemical cell performances of $Cu_2ZnSnSe_4$ thin films deposited on various conductive substrates. Vacuum 156, 172–180.

Hsu, W.C., Repins, I., Beall, C., Hart, C.D., Teeter, G., To, B., Yang, Y., Noufi, R., 2013. The effect of Zn excess on kesterite solar cells. Sol. Energy Mater. Sol. Cells 113, 160–164.

Juskenas, R., Niaura, G., Mockus, Z., Kanapeckaite, S., Giraitis, R., Kondrotas, R., Naujokaitis, A., Stalnionis, G., Pakstas, V., Karpaviciene, V., 2016. XRD studies of an electrochemically co-deposited Cu-Zn-Sn precursor and formation of a $Cu_2ZnSnSe_4$ absorber for thin-film solar cells. J. Alloys Compd. 655, 281–289.

Just, J., Sutter-Fella, C.M., Lützenkirchen-Hecht, D., Frahm, R., Schorr, S., Unold, T., 2016. Secondary phases and their influence on the composition of the kesterite phase in CZTS and CZTSe thin films. PCCP 18, 15988–15994.

Kaigawa, R., Hashimoto, S., Irago, T., Klenk, R., 2015. Direct preparation of $Cu_2ZnSnSe_4$ films by microwave irradiation and its dependence on the Sn/(Sn + Zn) ratio. Jpn. J. Appl. Phys. 54, 08KC02.

Kessler, F., Herrmann, D., Powalla, M., 2005. Approaches to flexible CIGS thin-film solar cells. Thin Solid Films 480–481, 491–498.

Khare, A., Himmetoglu, B., Johnson, M., Norris, D.J., Cococcioni, M., Aydil, E.S., 2012. Calculation of the lattice dynamics and Raman spectra of copper zinc tin chalcogenides and comparison to experiments. J. Appl. Phys. 111, 083707.

Kolesov, E.A., Tivanov, M.S., Korolik, O.V., Kapitanova, O.O., Dong, C.H., Won, K.T., Panin, G.N., 2019. Phonon anharmonicities in supported graphene. Carbon 141, 190–197.

Lafond, A., Choubrac, L., Guillot-Deudon, C., Deniard, P., Jobic, S., 2012. Crystal Structures of Photovoltaic Chalcogenides, an Intricate Puzzle to Solve: the Cases of CIGSe and CZTS Materials. Zeitschrift Für Anorganische Und Allgemeine Chemie 638 (15), 2571–2577.

Lifshin, E., 2008. X-ray Characterization of Materials. Wiley-VCH, Weinheim, pp. 1–261.

Lopez-Marino, S., Sánchez, Y., Espíndola-Rodríguez, M., Alcobé, X., Xie, H., Neuschitzer, M., Becerril, I., Giraldo, S., Dimitrievska, M., Placidi, M., Fourdrinier, L., Izquierdo-Roca, V., Pérez-Rodríguezad, A., Saucedoa, E., 2016. Alkali doping strategies for flexible and light-weight $Cu_2ZnSnSe_4$ solar cells. J. Mater. Chem. A 4 (5), 1895–1907.

Lu, D., Luo, S., Liu, S., Yao, H., Ren, X., Zhou, W., Tang, D., Qi, X., Zhong, J., 2018. Anomalous temperature-dependent Raman scattering of vapor deposited 2D Bi thin films. J. Phys. Chem. C 122 (42), 24459–24466.

Lutterotti, L., Matthies, S., Wenk, H.R., 1999. MAUD (Material Analysis Using Diffraction): a user friendly Java program for Rietveld Texture Analysis and more. In: Proceedings of the 12th International Conference on Textures of Materials (ICOTOM-12) 1, 1599.

Maeda, T., Nakamura, S., Wada, T., 2009. Phase stability and electronic structure of In-free photovoltaic semiconductors, Cu2ZnSnSe4 and Cu2ZnSnS4 by first-principles calculation. Mater. Res. Soc. Symp. Proc. 1165 1165-M04-03.

Marquez, J., Neuschitzer, M., Dimitrievska, M., Gunder, R., Haass, S., Werner, M., Romanyuk, Y.E., Schorr, S., Pearsall, N.M., Forbes, I., 2016. Systematic compositional changes and their influence on lattice and optoelectronic properties of $Cu_2ZnSnSe_4$ kesterite solar cells. Sol. Energy Mater. Sol. Cells 144, 579–585.

Márquez-Prieto, J., Ren, Y., Miles, R.W., Pearsall, N., Forbes, I., 2015. The influence of precursor Cu content and two-stage processing conditions on the micro-structure of $Cu_2ZnSnSe_4$. Thin Solid Films 582, 220–223.

Mortazavi Amiri, N.B., Postnikov, A., 2010. Electronic structure and lattice dynamics in kesterite-type $Cu_2ZnSnSe_4$ from first-principles calculations. Phys. Rev. B 82 (20) 205204.

Mousel, M., Redinger, A., Djemour, R., Arasimowicz, M., Valle, N., Dale, P., Siebentritt, S., 2013. HCl and Br 2-MeOH etching of C_u2ZnSnS_e4 polycrystalline absorbers. Thin Solid Films 535, 83–87.

Najmaei, S., Ajayan, Pulickel M., Lou, J., 2013. Quantitative analysis of the temperature dependency in Raman active vibrational modes of molybdenum disulfide atomic layers. Nanoscale 5, 9758–9763.

Otte, K., Makhova, L., Braun, A., Konovalov, I., 2006. Flexible Cu(In, Ga)S_e2 thin-film solar cells for space application. Thin Solid Films 511–512, 613–622.

Pagliaro, M., Palmisano, G., Ciriminna, R., 2008. Flexible Solar Cells. WILEY-VCH, Weinheim, pp. 1–30.

Rey, G., Redinger, A., Sendler, J., Weiss, T.P., Thevenin, M., Guennou, M., El Adib, B., Siebentritt, S., 2014. The band gap of $Cu_2ZnSnSe_4$: Effect of order-disorder. Appl. Phys. Lett. 105, 112106.

Salavei, A., Menossi, D., Piccinelli, F., Kumar, A., Mariotto, G., Barbato, M., Meneghini, M., Meneghesso, G., Mare, S.D., Artegiani, E., Romeo, A., 2016. Comparison of high efficiency flexible CdTe solar cells on different substrates at low temperature deposition. Sol. Energy 139, 13–18.

Salome, P.M.P., Fernandes, P.A., Leitao, J.P., Sousa, M.G., Teixeira, J.P., da Cunha, A.F., 2014. Secondary crystalline phases identification in $Cu_2ZnSnSe_4$ thin films: contributions from Raman scattering and photoluminescence. J. Mater. Sci. 49, 7425–7436.

Sarswat, P.K., Free, M.L., Tiwari, A., 2011. Temperature-dependent study of the Raman A mode of Cu_2ZnSnS_4 thin films. Phys. Status Solidi 248 (9), 2170–2174.

Schelhas, L.T., Stone, K.H., Harvey, S.P., Zakhidov, D., Salleo, A., Teeter, G., Repins, I.L., Toney, M.F., 2017. Point defects in $Cu_2ZnSnSe_4$ (CZTSe): resonant X-ray diffraction study of the low-temperature order/disorder transition. Phys. Status Solidi B 1700156.

Schorr, S., 2007. Structural aspects of adamantine like multinary chalcogenides. Thin Solid Films 515 (15), 5985–5991.

Schorr, S., Gurieva, G., Guc, M., Dimitrievska, M., Pérez-Rodríguez, A., Izquierdo-Roca, V., Schnohr, C.S., Kim, J., Jo, W., Merino, J.M., 2020. Point defects, compositional fluctuations, and secondary phases in non-stoichiometric kesterites. J. Phys. Energy 2, 012002.

Scragg, J.J.S., Larsen, J.K., Kumar, M., Persson, C., Sendler, J., Siebentritt, S., Bjorkman, C.P., 2015. Cu-Zn disorder and band gap fluctuations in Cu_2ZnSn(S, Se_y4: theoretical and experimental investigations. Phys. Status Solidi B 253 (2), 247–254.

Shockley, W., Queisser, H.J., 1961. Detailed balance limit of efficiency of p-n junction solar cells. J. Appl. Phys. 32 (3), 510–519.

Sim, J.H., Yang, K.J., 2017. The characteristics of flexible CZTSe. In: XXVI International Materials Research Congress, pp. SB.6-P031.

Sim, J.K., Kang, S., Nandi, R., Jo, J.Y., Jeong, K.U., Lee, C.R., 2018. Implementation of graphene as hole transport electrode in flexible CIGS solar cells fabricated on Cu foil. Sol. Energy 162, 357–363.

Singh, O.P., Muhunthan, N., Singh, V.N., Samanta, K., Dilawar, N., 2014. Effect of temperature on thermal expansion and anharmonicity in Cu_2ZnSnS_4 thin films grown by co-sputtering and sulfurization. Mater. Chem. Phys. 146 (3), 452–455.

Stanchik, A.V., Gremenok, V.F., Bashkirov, S.A., Tivanov, M.S., Juskenas, R.L., Novikov, G.F., Giraitis, R., Saad, A.M., 2018. Microstructure and Raman scattering of $Cu_2ZnSnSe_4$ thin films deposited onto flexible metal substrates. Semiconductors 52 (2), 215–220.

Stanchik, A.V., Gremenok, V.F., Juskenas, R.I., Tyukhov, I., Tivanov, M.S., Fettkenhauer, Ch., Shvartsman, V.V., Giraitis, R., Hagemann, U., Lupascu, D.C., 2019. Effects of

selenization time and temperature on the growth of $Cu_2ZnSnSe_4$ thin films on a metal substrate for flexible solar cells. Sol. Energy 178, 142–149.
Tampo, H., Kim, S., Nagai, T., Shibata, H., Niki, S., 2019. Improving the open circuit voltage through surface oxygen plasma treatment and 11.7% efficient $Cu_2ZnSnSe_4$ solar cell. ACS Appl. Mater. Interfaces 11 (14), 13319–13325.
Taube, A., Łapińska, A., Judek, J., Wochtman, N., Zdrojek, M., 2016. Temperature induced phonon behaviour in germanium selenide thin flms probed by Raman spectroscopy. J. Phys. D Appl. Phys. 49, 315301.
Valle Rios, L.E., Neldner, K., Gurieva, G., Schorr, S., 2016. Existence of off-stoichiometric single phase kesterite. J. Alloys Compd. 657, 408–413.
Vauche, L., Risch, L., Arasimowicz, M., Sánchez, Y., Saucedo, E., Pasquinelli, M., Goislard de Monsabert, T., Grand, P.-P., Jaime-Ferrer, S., 2016a. Detrimental effect of Sn-rich secondary phases on $Cu_2ZnSnSe_4$ based solar cells. J. Renew. Sustain. Energy 8 (3), 033502.
Vauche, L., Risch, L., Sanchez, Y., Dimitrievska, M., Pasquinelli, M., Goislard de Monsabert, T., Grand, P.-P., Jaime-Ferrer, S., Saucedo, E., 2016b. 8.2% pure selenide kesterite thin film solar cells from large area electrodeposited precursors. Prog. Photovoltics Res. Appl. 24 (1), 38–51.
Vora, N., Blackburn, J., Repins, I., Beall, C., To, B., Pankow, J., Teeter, G., Young, M., Noufi, R., 2012. Phase identification and control of thin films deposited by co-evaporation of elemental Cu, Zn, Sn, and Se. J. Vac. Sci. Technol., A 30 (5), 051201.
Wang, D., Zhao, J., Chen, B., Zhu, C., 2008. Lattice vibration fundamentals in nanocrystalline anatase investigated with Raman scattering. J. Phys.: Condens. Matter 20, 085212.
Wu, Y., An, M., Xiong, R., Shi, J., Zhang, Q.M., 2008. Raman scattering spectra in the normal phase of 2H–$NbSe_2$. J. Phys. D Appl. Phys. 41 (17), 175408.
Yan, Q., Cheng, S., Li, H., Yu, X., Fu, J., Tian, Q., Jia, H., Wu, S., 2019. High flexible $Cu_2ZnSn(S, Se)4$ solar cells by green solution-process. Sol. Energy 177, 508–516.
Yao, L., Ao, J., Jeng, M.-J., Bi, J., Gao, S., Sun, G., He, Q., Zhou, Z., Sun, Y., Chang, L.B., 2016. Effect of Sn content in a CuSnZn metal precursor on formation of $MoSe_2$ film during selenization in Se + SnSe vapor. Materials 9 (4), 241.
Yoo, H., Wibowo, R.A., Hölzing, A., Lechner, R., Palm, J., Jost, S., Gowtham, M., Sorin, F., Louis, B., Hock, R., 2013. Investigation of the solid state reactions by time-resolved x-ray diffraction while crystallizing kesterite $Cu_2ZnSnSe_4$ thin films. Thin Solid Films 535, 73–77.
Zhao, B., Tang, X.S., Huo, W.X., Jianga, Y., Ma, Z.G., Wang, L., Wang, W.X., Chen, H., Ji, H.Q., 2018. Characteristics of InGaP/GaAs double junction thin film solar cells on a flexible metallic substrate. Sol. Energy 174, 703–708.